Wall-modeled large-eddy simulation integrated with synthetic turbulence generator for mutiple-relaxation-time lattice Boltzmann method

(article starts on next page)

Wall-modeled large-eddy simulation integrated with synthetic turbulence generator for multiple-relaxation-time lattice Boltzmann method

Xue Xiao (薛骁) ✉ iD ; Yao Hua-Dong (姚华栋) iD ; Lars Davidson iD

Check for updates

CrossMark

View Online

Export Citation

AIP Publishing

Wall-modeled large-eddy simulation integrated with synthetic turbulence generator for multiple-relaxation-time lattice Boltzmann method

View Online   Export Citation   CrossMark

Xiao Xue (薛骁),[1,2,a] iD   Hua-Dong Yao (姚华栋),[1] iD   and Lars Davidson[1] iD

AFFILIATIONS

[1]Division of Fluid Dynamics, Department of Mechanics and Maritime Sciences, Chalmers University of Technology,
 41296 Gothenburg, Sweden
[2]Centre for Computational Science, Department of Chemistry, University College London, London, United Kingdom

[a]Author to whom correspondence should be addressed: xiaox@chalmers.se

ABSTRACT

The synthetic turbulence generator (STG) lies at the interface of the Reynolds averaged Navier–Stokes (RANS) simulation and large-eddy simulation (LES). This paper presents an STG for the multiple-relaxation-time lattice Boltzmann method (LBM) framework at high friction Reynolds numbers, with consideration of near-wall modeling. The Reichardt wall law, in combination with a force-based method, is used to model the near-wall field. The STG wall-modeled LES results are compared with turbulent channel flow simulations at $Re_\tau = 1000, 2000, 5200$ at different resolutions. The results demonstrate good agreement with direct numerical simulation, with the adaptation length of 6–8 boundary layer thickness. This method has a wide range of potentials for hybrid RANS/LES-LBM related applications at high friction Reynolds numbers.

I. INTRODUCTION

In industrial applications related to high Reynolds number flows, wall-bounded turbulence plays a crucial role in designing aircraft, cars, wind farms, and so on.[1] Direct numerical simulations (DNS) can accurately quantify the physics by solving the Navier–Stokes equations using high-order numerical approximations and grid refinement techniques.[2,3] However, DNS is computationally too expensive for real-world applications, making it impractical for use in the design cycle. Large-eddy simulations (LES) can reduce grid requirements by modeling subgrid-scale (SGS) eddy viscosity.[4–6] Nevertheless, LES still requires fine grid resolution in the near-wall region, requiring grid points to be proportional to $O(Re^n)$ with $n = 13/7$.[2,3,7] Wall-resolved LES (WRLES) is still far from an engineering tool.

To improve computational efficiency, studies have attempted to model the near-wall region by solving Reynolds-averaged Navier–Stokes (RANS) equations and using LES in the far field or by modeling the near-wall region with relatively few grids by reconstructing near-wall velocities. In past decades, the lattice Boltzmann method (LBM) has gained popularity for simulating fluid dynamic problems at a variety of scales, from micro–nanoscales[8–12] to macroscopic scales[13–17] at low Mach numbers. LBM offers an alternative to traditional methods by solving the Boltzmann equation at a mesoscopic level, instead of directly solving the Navier–Stokes equations.[16,18–20] LBM's parallelization-friendly nature makes it attractive due to the local update of discrete particle distribution functions. Hou et al.[13] introduced the effective turbulent viscosity to model the subgrid-scale (SGS) turbulence in the LBM framework. This approach combines the advantages of LES techniques with the computational efficiency of LBM.

To further improve computational efficiency, the hybrid RANS-LES approach is becoming increasingly popular as it balances accuracy and computational cost. The RANS method is used to conserve macroscopic quantities in computationally less-demanding regions, while LES provides detailed flow information in computationally-intensive areas. Generating high-quality turbulence at the RANS/LES interface is critical for achieving accurate results, as highlighted by Wu.[21] In the conventional computational fluid dynamics (CFD), studies have conducted wide range approaches by precursory DNS/LES data,[22] velocity

05 September 2023 10:30:05

field "recycling,"[23–25] synthetic eddy method (SEM),[26–28] or involving control techniques[29,30] to generate turbulence. Most of the existing studies suffer from either relatively long turbulent-developed adaptation length, high computational cost, or hard to generalize for complex geometries. Shur *et al.*[31] successfully developed a synthetic turbulent generator (STG) for the detached eddy simulation (DES).[32] The STG method creates velocity fluctuations based on the Fourier coefficients, which are given by the energy spectrum, whereas, for the SEM method, coherent structures are simulated by superimposing artificial eddies at the inlet plane. The results show both fast and robust with an adaption length of 2–4 boundary-layer widths.

Despite being an active area in the conventional CFD, studies using a turbulent generator in the LBM framework are still rare. Koda and Lien[33] generated turbulence for the channel flow by placing a "recycled" channel flow before the inlet, which requires a pre-simulated periodic turbulent channel flow. Nakayama *et al.*[34] used the similar recycling approach and additionally added a heat flux source from the realistic observation to simulate atmospheric flow over a city. Asmuth *et al.*[35] applied pre-synthetic turbulence inflow for the wind farm simulation. The above-mentioned methods need additional preparation work for the inlet turbulence before applying it to the applications. Buffa *et al.*[36] reconstructed turbulence by using the SEM method in LBM (SEM-LBM); however, this method may suffer from a relatively long adaptation length.[37] Xue *et al.*[38] integrated the synthetic turbulent generator (STG) in the LBM framework at $Re_\tau = 180$ with wall-resolved LES-LBM simulation with an adaptation length of 2–4 boundary-layer widths. However, the friction Reynolds number is relatively low and the Bhatnagar–Gross–Krook (BGK) collision operator limited its applications for high Reynolds number cases. To reduce computational time and maintain STG accuracy, modeling the near-wall flow field with a wall-model (WM) in the LES-based LBM (WMLBM) is a non-straightforward task. The first WMLBM was proposed by Malaspinas and Sagaut[39] where they successfully reconstructed the first-layer near-wall velocity with the Musker wall function or log-law (see Ref. 40). Then, follow-up works came up with the idea of reconstructing the velocity field or modeling the velocity bounce back.[39,41–44] However, the force-based method is rarely mentioned or described in detail in the LBM framework.[45]

In the present work, a synthetic turbulent generator is developed, integrated with a multiple-relaxation-time (MRT) LBM collision operator to tackle high friction Reynolds numbers. The near-wall region is modeled via a force-based wall model, using a wall law by Reichardt (see Ref. 46). The performance of the STG method is examined at three different friction Reynolds numbers: $Re_\tau = 1000$, $Re_\tau = 2000$, and $Re_\tau = 5200$ at various resolutions, and compared with DNS data from Hoyas and Lee (see Refs. 47 and 48). The proposed framework aims to produce high-quality turbulence at the RANS/LES-LBM interface to cater to high Reynolds number flow applications.[1,49,50]

II. METHODOLOGY

A. The multiple-relaxation-time lattice Boltzmann method

In this work, we utilize a three-dimensional (3D) lattice model with 19 discretized directions known as the D3Q19 model. The lattice cell is located at position **x** and time t, with a discretized velocity set $\mathbf{c}_i$ for $i \in 0, 1, \ldots, Q-1$ ($Q = 19$)

$$\mathbf{c}_i = \{(0, -1, -1), (-1, 0, -1), (0, 0, -1), (1, 0, -1),$$
$$(0, 1, -1), (-1, -1, 0), (0, -1, 0), (1, -1, 0), (-1, 0, 0),$$
$$(0, 0, 0), (1, 0, 0), (-1, 1, 0), (0, 1, 0), (1, 1, 0), (0, -1, 1),$$
$$(-1, 0, 1), (0, 0, 1), (1, 0, 1), (0, 1, 1)\}. \tag{1}$$

The weight for the discretized directions is defined as

$$w_9 = \frac{1}{3}, \quad w_{2,6,8,10,12,16} = \frac{1}{18}, \quad w_{0,1,3,4,5,7,11,13,14,15,17,18} = \frac{1}{36}. \tag{2}$$

The evolution equation for the distribution functions, accounting for collision and forcing, can be expressed as

$$\mathbf{f}(\mathbf{x} + \mathbf{c}_i \Delta t, t + \Delta t) = \mathbf{f}(\mathbf{x}, t) - \Omega[\mathbf{f}(\mathbf{x}, t) - \mathbf{f}^{eq}(\mathbf{x}, t)] + \mathbf{F}(\mathbf{x}, t)\Delta t, \tag{3}$$

where Ω is a collision kernel and Δt is the lattice Boltzmann time step, which is set to unity. In this work, MRT collision kernel is chosen due to its higher numerical stability compared to the BGK model at high Reynolds numbers[51]

$$\Omega = \mathbf{M}^{-1}\mathbf{S}\mathbf{M}, \tag{4}$$

where **M** is the transformation matrix from the population space to the moment space obtained via the Gram–Schmidt approach [**M** matrix is described in Eq. (A1)]. **S** is the diagonal matrix with relaxation frequencies at different moments, $\mathbf{S} = diag\{\omega_0, \omega_1, \ldots, \omega_{Q-1}\}$, MRT collision operator will be equivalent to BGK with ω_i set to the same value ω. The frequency ω_i is the inverse of the relaxation time τ_i. Note that we set $\tau_k = \tau_9 = \tau_{11} = \tau_{13} = \tau_{14} = \tau_{15}$, which are related to the kinematic viscosity ν, which is

$$\nu = c_s^2 \left(\tau_k - \frac{1}{2}\right)\Delta t \tag{5}$$

with c_s being the speed of the sound, and c_s^2 is equal to 1/3 lattice Boltzmann unit (LBU). Other relaxation parameters can be found in Eqs. (A2)–(A6). Instead of colliding in the population space, the MRT collides in the moment space; thus, Eq. (3) can be rewritten as

$$\mathbf{f}(\mathbf{x} + \mathbf{c}_i \Delta t, t + \Delta t) = \mathbf{f}(\mathbf{x}, t) - \mathbf{M}^{-1}\mathbf{S}[\mathbf{m}(\mathbf{x}, t) - \mathbf{m}^{eq}(\mathbf{x}, t)]$$
$$+ \mathbf{F}(\mathbf{x}, t)\Delta t, \tag{6}$$

where **m** is the moment space component, which is defined as

$$\mathbf{m}(\mathbf{x}, t) = \mathbf{M}\mathbf{f}(\mathbf{x}, t). \tag{7}$$

The moment space equilibrium $\mathbf{m}^{eq}(\mathbf{x}, t)$ can be defined as

$$\mathbf{m}_0^{eq} = \rho, \quad \mathbf{m}_1^{eq} = -11\rho + 19\rho(u_x^2 + u_y^2 + u_z^2),$$

$$\mathbf{m}_2^{eq} = \frac{11}{2}\rho\left(3 - (u_x^2 + u_y^2 + u_z^2)\right), \quad \mathbf{m}_3^{eq} = \rho u_x,$$

$$\mathbf{m}_4^{eq} = -\frac{3}{2}\rho u_x, \quad \mathbf{m}_5^{eq} = \rho u_y, \quad \mathbf{m}_6^{eq} = -\frac{3}{2}\rho u_y,$$

$$\mathbf{m}_7^{eq} = \rho u_z, \quad \mathbf{m}_8^{eq} = -\frac{3}{2}\rho u_z, \quad \mathbf{m}_9^{eq} = 2\rho u_x^2 - \rho u_y^2 - \rho u_z^2, \tag{8}$$

$$\mathbf{m}_{10}^{eq} = -\rho u_x^2 + \frac{1}{2}\rho u_y^2 + \frac{1}{2}\rho u_z^2, \quad \mathbf{m}_{11}^{eq} = \rho u_y^2 - \rho u_z^2,$$

$$\mathbf{m}_{12}^{eq} = -\frac{1}{2}\rho u_y^2 + \frac{1}{2}\rho u_z^2, \quad \mathbf{m}_{13}^{eq} = \rho u_x u_y, \quad \mathbf{m}_{14}^{eq} = \rho u_y u_z,$$

$$\mathbf{m}_{15}^{eq} = \rho u_x u_z, \quad \mathbf{m}_{16}^{eq} = \mathbf{m}_{17}^{eq} = \mathbf{m}_{18}^{eq} = 0.$$

$\mathbf{F}(\mathbf{x}, t)$ in Eq. (6) is the vector of $F_i(\mathbf{x}, t)$, which is the volume force acting on the fluid cell[52]

$$F_i(\mathbf{x}, t) = \left(1 - \frac{\omega_i}{2}\right) w_i \left[\frac{\mathbf{c}_i - \mathbf{u}(\mathbf{x}, t)}{c_s^2} + \frac{\mathbf{c}_i \cdot \mathbf{u}(\mathbf{x}, t)}{c_s^4} \mathbf{c}_i\right] \cdot \mathbf{g}, \quad (9)$$

where $\mathbf{g}$ is the volume acceleration. The macro-scale quantities for the density, momentum, and momentum flux tensors can be calculated from the distribution function, the discrete velocities, and the volume force

$$\rho(\mathbf{x}, t) = \sum_{i=0}^{Q-1} f_i(\mathbf{x}, t), \quad (10)$$

$$\rho(\mathbf{x}, t)\mathbf{u}(\mathbf{x}, t) = \sum_{i=0}^{Q-1} f_i(\mathbf{x}, t)\mathbf{c}_i + \frac{1}{2}\mathbf{g}\Delta t, \quad (11)$$

$$\mathbf{\Pi}(\mathbf{x}, t) = \sum_{i=0}^{Q-1} f_i(\mathbf{x}, t)\mathbf{c}_i\mathbf{c}_i. \quad (12)$$

Note that the momentum flux, $\mathbf{\Pi}(\mathbf{x}, t)$, can be presented by the sum of the equilibrium and non-equilibrium parts, $\mathbf{\Pi}(\mathbf{x}, t) = \mathbf{\Pi}_{\text{eq}}(\mathbf{x}, t) + \mathbf{\Pi}_{\text{neq}}(\mathbf{x}, t)$.

B. Smagorinsky subgrid-scale modeling

In this part, the lattice-Boltzmann-based Smagorinsky SGS large-eddy simulation techniques are summarized. In the LBM framework, the effective viscosity ν_{eff}[3,13,33] is modeled as the sum of the molecular viscosity ν_0 and the turbulent viscosity ν_t

$$\nu_{\text{eff}} = \nu_0 + \nu_t, \quad \nu_t = C_{\text{smag}}\Delta^2|\bar{\mathbf{S}}|, \quad (13)$$

where $|\bar{\mathbf{S}}|$ is the filtered strain rate tensor

$$|\bar{\mathbf{S}}| = \frac{-\tau_i\rho\Delta x^2/\Delta t + \sqrt{(\tau_i\rho)^2\Delta x^4/\Delta t^2 + 18\sqrt{2}\rho C_{\text{smag}}\delta^2 Q^{1/2}}}{6\rho C_{\text{smag}}\Delta^2}, \quad (14)$$

where C_{smag} is the Smagorinsky constant, Δ represents the filter size, and τ_i is the relaxation time for the moment-space collision. $Q^{1/2}$ is $Q^{1/2} = \sqrt{\mathbf{\Pi}_{\text{neq}} : \mathbf{\Pi}_{\text{neq}}}$, with $\mathbf{\Pi}_{\text{neq}}$ being the non-equilibrium part of the momentum flux tensor shown in Eq. (12). With the help of Eq. (5), the total relaxation time τ_{eff} is obtained as

$$\tau_i^{\text{eff}} = \frac{\tau_i}{2} + \frac{\sqrt{(\tau_i\rho\Delta x/\Delta t)^2 + 18\sqrt{2}C_{\text{smag}}Q^{1/2}}}{2\rho c}. \quad (15)$$

Finally, τ_i^{eff} is replaced by the related MRT collision operator relaxation τ_i to enclose the lattice-Boltzmann-based LES system.

C. Near-wall modeling for LBM

There have been various approaches in the LBM framework to model the near-wall field with a wall model. Most of them are based on the reconstruction of near-wall populations to preserve the velocity and density fields or bounce-back approach to preserve the target velocity.[39,41–44,53] Reference 39 also coupled a RANS solver at the near-wall region with LBM; however, it is proven to be more time

consuming than a monolithic LBM method. In the present work, we focus on developing a wall model that is based on forces in the near-wall region.

In this paper, the Reichardt wall law[46] will be used instead of the one from Musker.[40] Similar to the Musker law, the Reichardt wall law covers the buffer zone and gives the full prediction of the u^+ as a function of y^+, where the other wall law needs different expressions at different zones. Detailed discussions regarding wall function prediction errors can be found at Haussmann et al.[41] The Reichardt wall law shown in Fig. 1 is defined as

$$u^+ = 2.5\ln(1 + 0.4y^+) + 7.8(1 - e^{-y^+/11}) - y^+ e^{-y^+/3}, \quad (16)$$

where u^+ and y^+ are the dimensionless unit defined as

$$u^+ = \frac{\langle u \rangle}{u_\tau}, \quad y^+ = yu_\tau/\nu, \quad (17)$$

where u_τ is the shear velocity, $u_\tau = \sqrt{\tau_w/\rho}$, $\langle \cdot \rangle$ denotes ensemble average over space or time, τ_w is the wall shear stress, and u is the streamwise velocity. Figure 2 illustrates the use of a slip wall boundary condition for the wall treatment. Notice that, the force-based model was also mentioned in Kuwata and Suga[45] as the "wall function with specular reflection conditions." To generalize the wall model, a base vector $\mathbf{e}_x$ is first needed to project the near-wall velocity $\mathbf{u}_w$ on the wall-parallel direction

$$\mathbf{e}_x = \frac{\mathbf{u}_2 - (\mathbf{u}_2 \cdot \mathbf{n})\mathbf{n}}{\|\mathbf{u}_2 - (\mathbf{u}_2 \cdot \mathbf{n})\mathbf{n}\|}, \quad (18)$$

where $\mathbf{u}_2$ is the velocity in the second cell from the wall and $\mathbf{n}$ is the wall-normal vector. Then, we project the velocity in the first cell near the wall, $\mathbf{u}_w$, to obtain the scalar streamwise velocity, $\hat{u}_w$, which is defined as

$$\hat{u}_w = \mathbf{u}_w \cdot \mathbf{e}_x. \quad (19)$$

Next, the aim is to compute the friction velocity u_τ by solving for u_τ in Eq. (16)

$$u_\tau(\mathbf{x}, t) = u^+(y_\perp(\mathbf{x}, t), \hat{u}_w(\mathbf{x}, t), u_\tau(\mathbf{x}, t)). \quad (20)$$
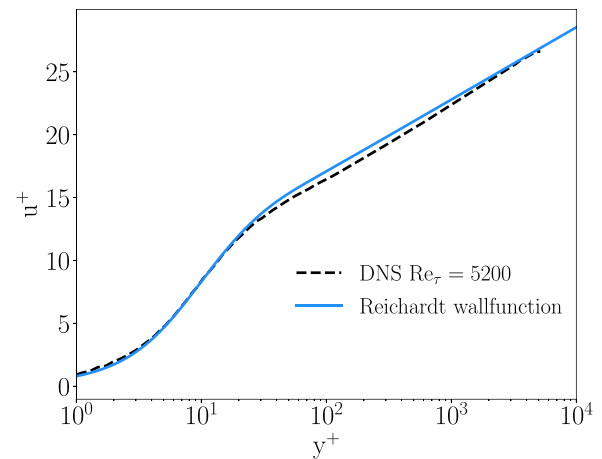

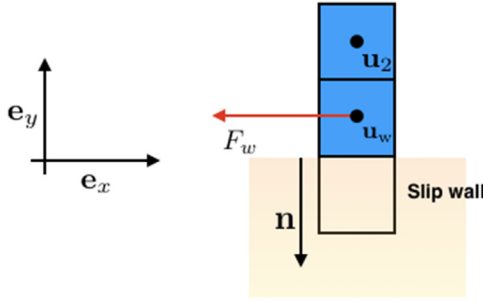**FIG. 1.** Reichardt's wall law from $y^+ = 1$ to $y^+ = 10\,000$.

FIG. 2. Sketch on the first layer near the wall.

By using the Newton method, we update the friction velocity locally. Note that, instead of using a plane averaged friction velocity,[41] this work uses the local value to make the algorithm more generalized. The wall shear stress can be estimated by $\tau_w(\mathbf{x}, t) = u_\tau^2(\mathbf{x}, t)\rho(\mathbf{x}, t)$. Finally, the force near the wall is defined as

$$F_w(\mathbf{x}, t) = -\tau_w(\mathbf{x}, t)A, \tag{21}$$

where F is the shear force acting on the wall. A notable advantage of the force-based method is that it does not require any reconstruction of populations to find the target velocity and density near the wall, making it easier to implement compared to other wall modeling methods.

III. SYNTHETIC TURBULENCE GENERATOR FOR THE WALL-MODELED LATTICE BOLTZMANN METHOD

A. Synthetic turbulence generator formulation in LBM framework

In this study, a synthetic turbulence generator (STG) is positioned at the inlet of a channel flow. It needs velocity field from a $k - \omega$ RANS simulation.[54] The total velocity $\mathbf{u}_{in}(\mathbf{x}, t)$ at the inlet is given by

$$\mathbf{u}_{in}(\mathbf{x}, t) = \mathbf{u}_{RANS}(\mathbf{x}) + \mathbf{u}'(\mathbf{x}, t), \tag{22}$$

where $\mathbf{u}_{RANS}$ is the velocity vector obtained from a RANS simulation; then, the interpolated velocity will be applied on the LBM grid in the case of grid resolution differences.[38] The STG generates the velocity fluctuations $\mathbf{u}'(\mathbf{x}, t)$ at the cell $\mathbf{x}$ at time t

$$\mathbf{u}'(\mathbf{x}, t) = a_{\alpha\beta}\mathbf{v}'(\mathbf{x}, t). \tag{23}$$

The time-averaged velocity fluctuation is zero, i.e., $\langle\mathbf{u}'(\mathbf{x}, t)\rangle = 0$. The Cholesky decomposition of the Reynolds stress tensor reads

$$\{a_{\alpha\beta}\} = \begin{pmatrix} \sqrt{R_{11}} & 0 & 0 \\ R_{21}/a_{11} & \sqrt{R_{22} - a_{21}^2} & 0 \\ R_{31}/a_{11} & (R_{32} - a_{21}a_{31})/a_{22} & \sqrt{R_{33} - a_{31}^2 - a_{32}^2} \end{pmatrix}, \tag{24}$$

where $R_{\alpha\beta} = \langle u'_\alpha u'_\beta \rangle$ is taken from the Reynolds stress tensor using EARSM[55] when post-processing the 1D RANS data. $\mathbf{v}'(\mathbf{x}, t)$ in Eq. (23) is imposed by N Fourier modes given by

$$\mathbf{v}'(\mathbf{x}, t) = \sqrt{6}\sum_{n=1}^{N}\sqrt{q^n}[\boldsymbol{\sigma}^n\cos(k^n\mathbf{d}^n\cdot\mathbf{x}' + \phi^n)], \tag{25}$$

where q^n is the amplitude of a modified von Karman spectrum, n is the mode number, k^n is the amplitude of the mode direction vectors $\mathbf{d}^n$ with $\boldsymbol{\sigma}^n\cdot\mathbf{d}^n = 0$, ϕ^n is the random mode phase that is uniformly distributed in the interval of $[0, 2\pi)$. A detailed description is found in Refs. 31 and 38. The distribution function at the inlet of the channel flow can be defined as the sum of equilibrium part and the non-equilibrium part

$$f_i^{in}(\mathbf{x}, t) = f_i^{in(eq)}(\mathbf{x}, t) + f_i^{in(neq)}(\mathbf{x}, t), \tag{26}$$

where $f_i^{in(eq)}(\mathbf{x}, t)$ is the equilibrium part of the inlet distribution function, which can be calculated by

$$f_i^{in(eq)}(\mathbf{x}, t) = w_i\rho_{in}(\mathbf{x}, t)\left[1 + \frac{\mathbf{c}_i\cdot\mathbf{u}_{in}(\mathbf{x}, t)}{c_s^2} + \frac{[\mathbf{c}_i\cdot\mathbf{u}_{in}(\mathbf{x}, t)]^2}{2c_s^4} - \frac{[\mathbf{u}_{in}(\mathbf{x}, t)\cdot\mathbf{u}_{in}(\mathbf{x}, t)]}{2c_s^2}\right]. \tag{27}$$

ALGORITHM 1. STG-WMLBM: Implementation of synthetic turbulence generator for the MRT wall-modeled LBM.

---

1. Obtain the RANS velocity at the inlet $\mathbf{u}_{RANS}(\mathbf{x})$ in Eq. (22).
2a. Read saved value from the RANS simulation: $R_{\alpha\beta}$, k, ω field, etc.
2b. Compute the Reynolds stresses using EARSM
3. Calculate $a_{\alpha\beta}$ with the help of Eq. (24).
for all t from 0 to t_{end} **do**
　for all cells **do**
　　if cell $\mathbf{x}$ is at the RANS/LBM inlet **then**
　　　4. Calculate $\mathbf{v}'(\mathbf{x}, t)$ from Eq. (25).
　　　5. Compute the fluctuating velocity $\mathbf{u}'(\mathbf{x}, t)$ following Eqs. (23) and (24), respectively.
　　　6. Compute boundary density $\rho_{in}(\mathbf{x}, t)$ thanks to Eq. (30).
　　　7. Reconstruct the particle's probability distribution function by combining Eqs. (26)–(28).
　　　8. Update the LES–LBM relaxation time for the MRT framework t_{eff} in Eq. (15) and replace in kinematic-viscosity-related relaxation time in Eq. (5).
　　end if
　　if cell $\mathbf{x}$ is at the wall function cell **then**
　　　9. Compute $\mathbf{u}_2$.
　　　10. Compute the wall-parallel base vector $\mathbf{e}_x$ with the help of Eq. (18).
　　　11. Compute the scalar streamwise velocity $\hat{u}_w$ using Eq. (19).
　　　12. Solve implicit function to obtain u_τ with the help of Eqs. (20) and (16).
　　　13. Compute τ_w with the help of $\tau_w(\mathbf{x}, t) = u_\tau^2(\mathbf{x}, t)\rho(\mathbf{x}, t)$.
　　　14. Update force on the cell $F_w(\mathbf{x}, t)$ by using Eq. (21)
　　end if
　　15. Apply stream and collide with the consideration of forces to update the $f_i(\mathbf{x}, t)$ at each cell Eq. (3)
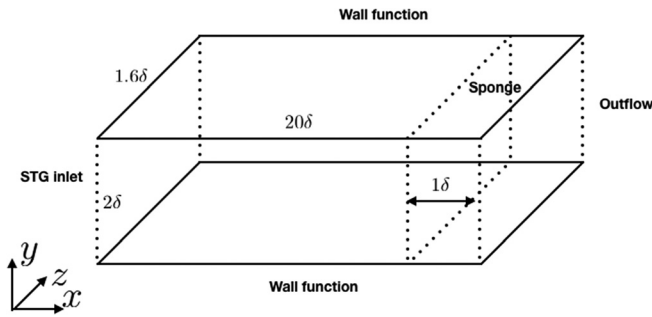　**end for**
end for

FIG. 3. Numerical setup of the channel flow simulation.

Following the regularized scheme,[56] the non-equilibrium part of the inlet distribution function in Eq. (26) is obtained via

$$f_i^{\text{in(neq)}}(\mathbf{x}, t) \approx \frac{w_i}{c_s^4} \mathbf{Q}_i : \boldsymbol{\Pi}_{\text{neq}}^{\text{in}}, \qquad (28)$$

where $\mathbf{Q}_i = \mathbf{c}_i \mathbf{c}_i - c_s^2 \mathbf{I}$ with $\mathbf{I}$ being the identity matrix. $\boldsymbol{\Pi}_{\text{neq}}^{\text{in}}$ is the non-equilibrium part of the moment flux tensor, which is defined as

$$\boldsymbol{\Pi}_{\text{neq}} = \sum_{i=0}^{Q-1} \mathbf{Q}_i f_i^{\text{in(neq)}}(\mathbf{x}, t). \qquad (29)$$

The unknown variables in the ith direction at the inlet can be calculated via the known direction following $\mathbf{Q}_i = \bar{\mathbf{Q}}_{\text{inv}(i)}$, $f_i^{\text{in(neq)}}(\mathbf{x}, t) = \bar{f}_{\text{inv}(i)}^{\text{in(neq)}}(\mathbf{x}, t)$, where the notation "inv" denotes the opposite direction of the unknown variable. For the density of the inlet boundary, we follow the idea from[57]

$$\rho_{\text{in}}(\mathbf{x}, t) = \frac{1}{1 + \hat{u}_{\text{in}}(\mathbf{x}, t)} (2\rho_\perp(\mathbf{x}, t) + \rho_\parallel(\mathbf{x}, t)), \qquad (30)$$

where $\hat{u}_{\text{in}}$ is the cross product with the normal unit vector $\mathbf{n}$ at the boundary $\hat{u}_{\text{in}} = \mathbf{u}_{\text{LB}}^{\text{in}} \cdot \mathbf{n}(|\hat{u}_{\text{in}}| < 0.3c_s)$ and $\mathbf{u}_{\text{LB}}^{\text{in}}$ is the velocity of the lattice Boltzmann domain at the interface. $\rho_\perp$ and $\rho_\parallel$ are the density calculated by

$$\rho_\perp(\mathbf{x}, t) = \sum_{i \in \{i | \mathbf{c}_i \cdot \mathbf{n}' = 0\}} f_i^\perp(\mathbf{x}, t), \quad \rho_\parallel(\mathbf{x}, t) = \sum_{i \in \{i | \mathbf{c}_i \cdot \mathbf{n}' < 0\}} f_i^\parallel(\mathbf{x}, t), \qquad (31)$$

where $\mathbf{n}'$ is the normal vector pointing toward the inlet boundary, $f_i^\perp$ and $f_i^\parallel$ are the probability density functions that point toward the boundary and are parallel to the boundary.

B. Implementation summary

In Algorithm 1, we summarize the implementation details of STG in the WMLBM framework.
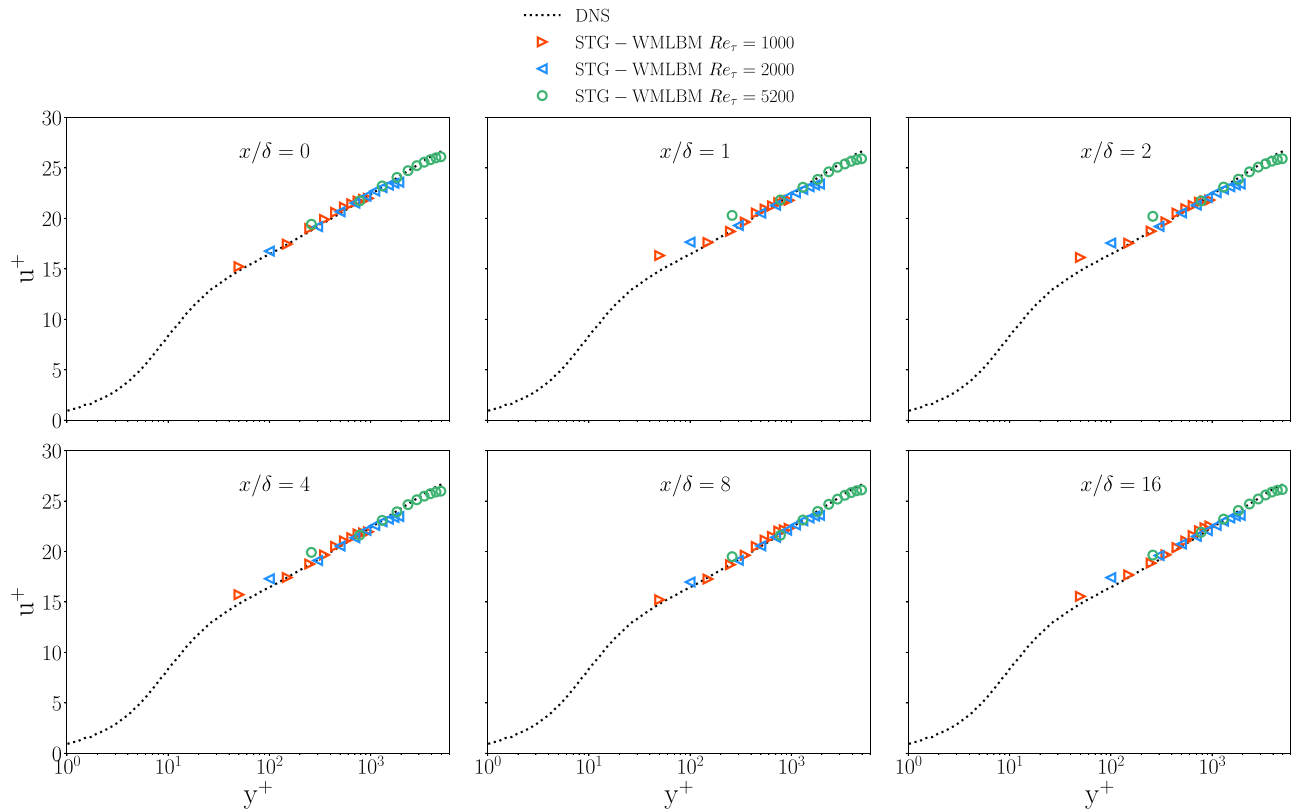
FIG. 4. u^+ as a function of y^+ at $Re_\tau = 1000, 2000, 5200$ for $H = 20$ (LBU).

IV. TURBULENT CHANNEL FLOW SIMULATIONS

This section presents the turbulent channel flow simulations with the STG as the inlet at $Re_\tau = 1000$, $Re_\tau = 2000$, and $Re_\tau = 5200$. The present work employs three different resolutions, LBU, in reference to the height of the channel H, that is, LBU = $H/20$, $H/40$, and $H/60$.

A. Numerical setup

The turbulent channel flow simulations use STG at the inlet and a pressure-free in the streamwise direction at the outlet. Periodic boundary conditions are employed in the spanwise direction (z) and wall functions are used at the first cell-layer near the top and bottom (y) planes, which are equipped with the slip boundary condition. To minimize the reflection wave's impact on the flow field, a sponge zone is placed near the outlet.[38] The numerical setup for the channel flow is depicted in Fig. 3, where the boundary layer thickness (δ) is defined as half of the channel height. The extent of the simulation domain is $20\delta \times 2\delta \times 1.6\delta$ in the x, y, and z directions, respectively. The sponge layer thickness is set to 1δ. The Smagorinsky constant is set to $C_{smag} = 0.01$. The simulations are conducted at different friction Reynolds numbers and resolutions, and run for a total of 10 domain-through times ($10T$). It is worth mentioning that the time convergence study of the STG has been addressed in our previous work (see Ref. 38). The present study finds that the turbulent statistics is stabilized after two domain-through times ($2T$). Thus, all statistical analyses begin after $2T$.

B. Results

This work presents validation of the STG framework for high friction Reynolds numbers, i.e., $Re_\tau = 1000$, $Re_\tau = 2000$, and $Re_\tau = 5200$. The initial investigation focuses on the resolution with $H = 2\delta = 20$ LBU. The y^+ values at $H = 20$ LBU for $Re_\tau = 1000$, 2000, and 5200 are approximately 50, 100, and 260, respectively. The results, triggered by the STG inlet, are compared with DNS data.[47,48]

Figure 4 shows the mean velocity field of u^+ as a function of y^+. The STG-WMLBM results compare with the DNS data at different friction Reynolds numbers. The results of the STG-WMLBM at all three friction Reynolds numbers show good agreement with DNS reference starting from $x/\delta = 0$. While the initial results are promising, further investigations are needed to analyze the Reynolds stresses in order to fully evaluate the effectiveness of the method. Figure 5 depicts the representation of $\langle u'u' \rangle^+$ as a function of y/δ for different values of the friction Reynolds number (Re_τ), namely, $Re_\tau = 1000, 2000, 5200$. The results obtained from STG-WMLBM have been compared against the DNS data to validate the accuracy of the LBM approach. At the initial stages of the flow, the LBM results display substantial deviations from the DNS data between the locations $x/\delta = 0$ and $x/\delta = 4$, since the turbulence in the flow has not yet fully developed. However, as the flow progresses downstream, these discrepancies reduce and the LBM results converge toward the DNS reference. By $x/\delta = 8$, the LBM results have stabilized and show good agreement with the DNS data, demonstrating the effectiveness of the LBM approach in predicting the turbulent flow characteristics.
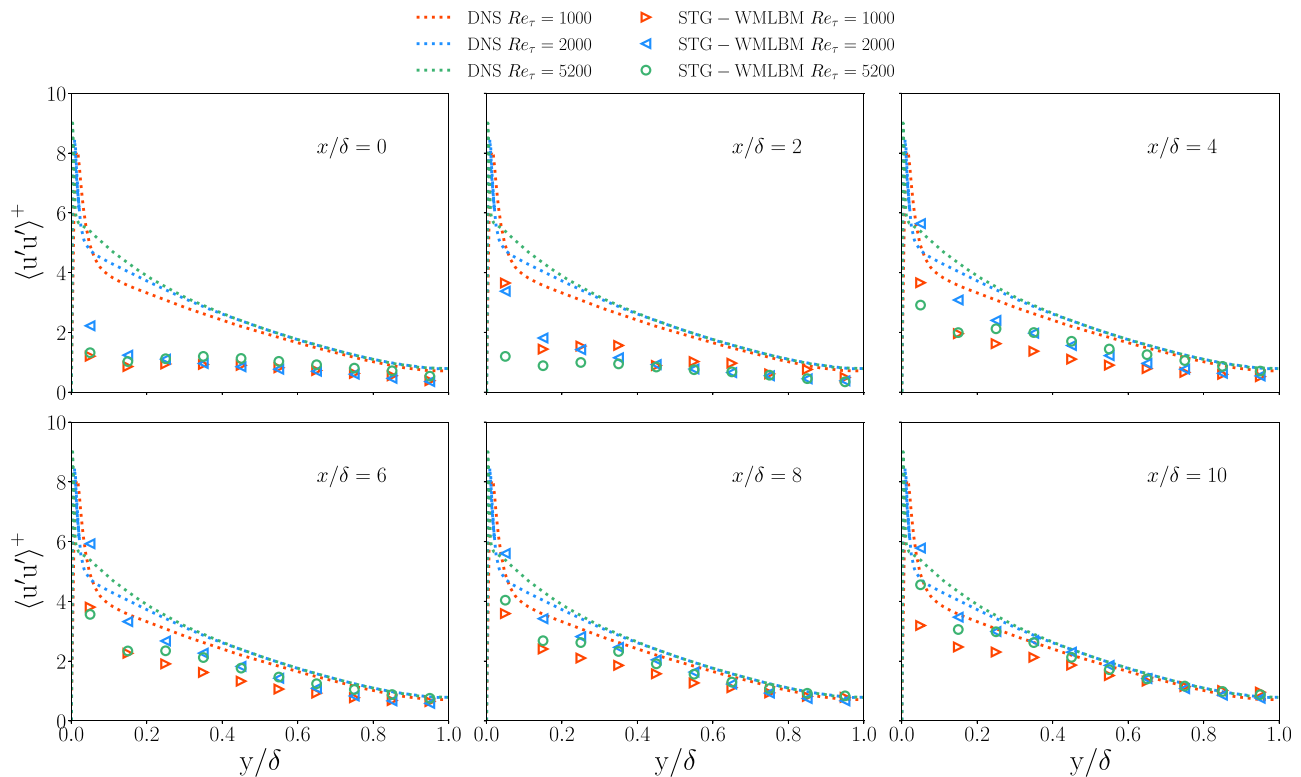
FIG. 5. $\langle u'u' \rangle^+$ as a function of y/δ at $Re_\tau = 1000, 2000, 5200$ for $H = 20$ (LBU).
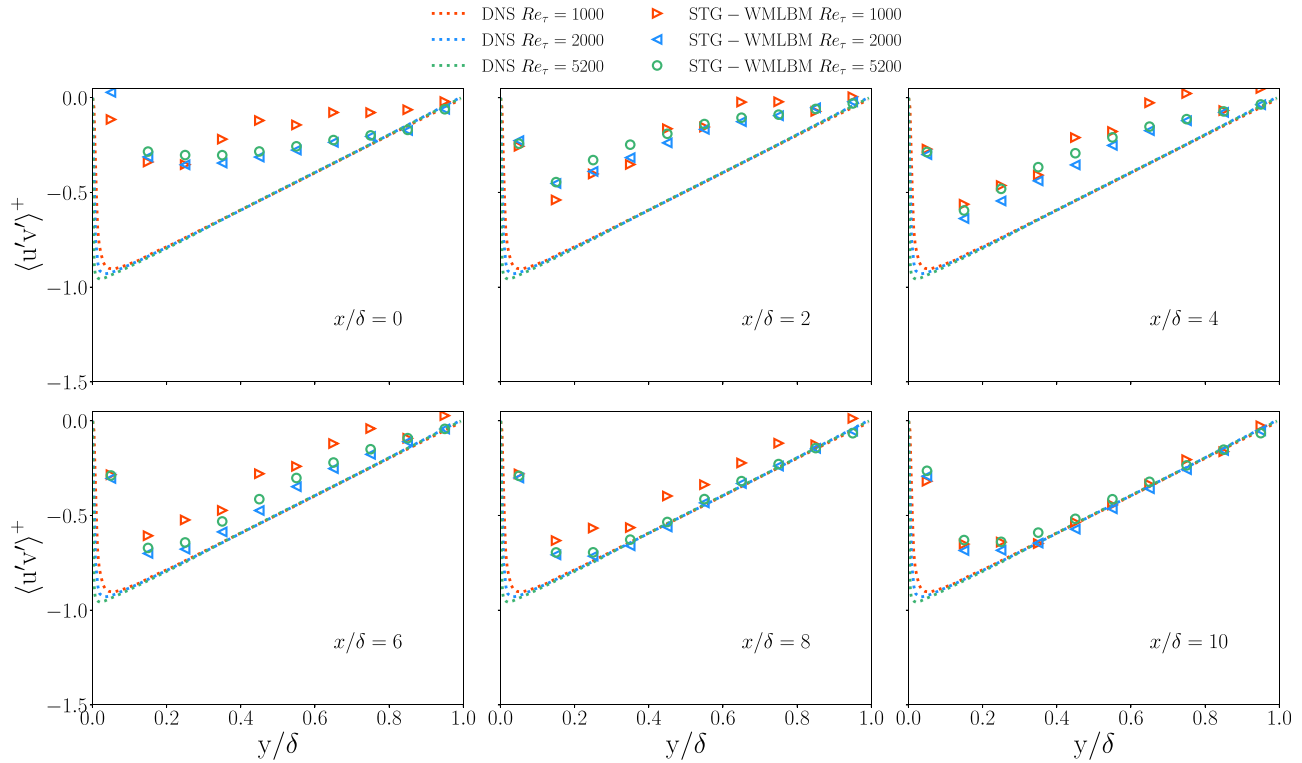
FIG. 6. $\langle u'v' \rangle^+$ as a function of y/δ at $Re_\tau = 1000, 2000, 5200$ for $H = 20$ (LBU).

Then, this work also examines the convergence of the algorithm by investigation on the comparison of $\langle u'v' \rangle^+$ between STG-WMLBM and DNS. Figure 6 shows $\langle u'v' \rangle^+$ as a function of y/δ. The STG-WMLBM results compare with the DNS data at different friction Reynolds numbers. For $Re_\tau = 2000$ and 5200, the STG-WMLBM results exhibit excellent agreement with the DNS reference data after $x/\delta = 6 - 8$. Meanwhile, for $Re_\tau = 1000$, the results converge to the DNS data at approximately $x/\delta = 8$–10. However, discrepancies with the DNS data are observed near the wall, which can be attributed to the poor resolution.

To further analyze the downstream development of the turbulence, the present work calculates the normalized mean absolute error (nMAE) between the STG-WMLBM and DNS, which is defined as

$$\text{nMAE} := \frac{\sum_{i=1}^{m} |y_{i,\text{LBM}} - y_{i,\text{DNS}}|}{\sum_{i=1}^{m} y_{i,\text{DNS}}}, \quad (32)$$

where m is the total number of the data points from the results, and $y_{i,\text{LBM}}$ and $y_{i,\text{DNS}}$ are the y axis data for LBM results and DNS reference, respectively. Figure 7 illustrates nMAE of $\langle u'u' \rangle^+$ along the downstream direction from the inlet to the outlet. The trend observed
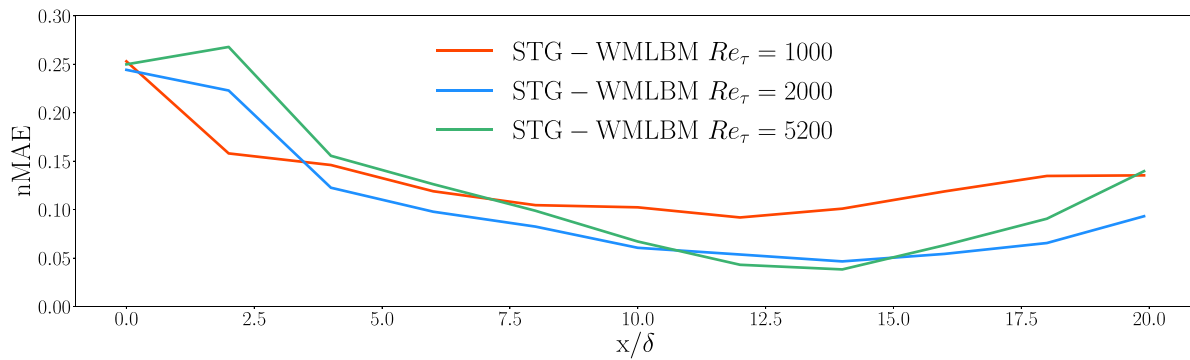

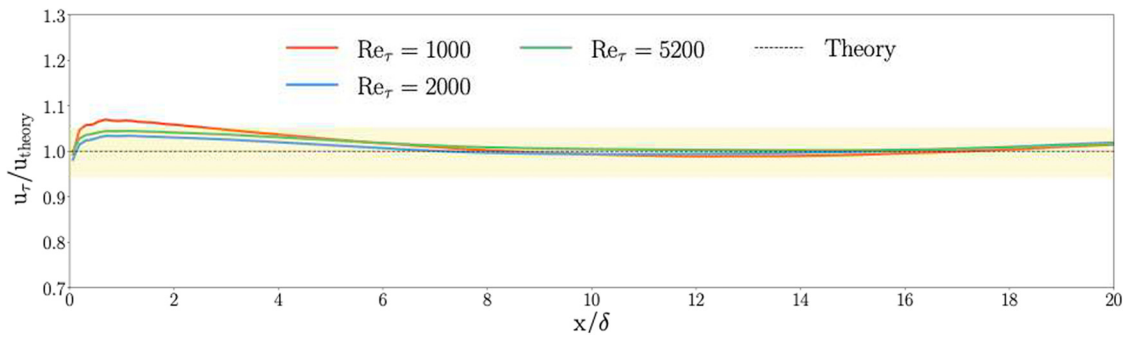**FIG. 7.** nMAE of $\langle u'u' \rangle^+$ as a function of x/δ at $Re_\tau = 1000, 2000, 5200$ for $H = 20$ (LBU).

FIG. 8. Normalized u_τ/u_{theory} as a function of x/δ at $Re_\tau = 1000, 2000, 5200$ for $H = 20$ (LBU).

in the figure clearly demonstrates the level of agreement between the LBM results and the DNS data at different x/δ. The error in the LBM results is observed to be in good agreement with the DNS data around $x/\delta = 8$. This indicates that the LBM approach has effectively captured the turbulence characteristics in the flow near this location. The error then stabilizes until $x/\delta = 15$, confirming the robustness of the LBM approach in the intermediate region of the flow. However, near the outlet, the error is observed to increase due to the presence of the buffer layer. This is a common phenomenon in turbulence simulations, as the buffer layer is known to have a significant impact on the

accuracy of the simulation results. Nevertheless, the figure highlights the overall reliability of the STG-WMLBM approach in predicting the turbulence characteristics in the flow.

Next, we will present the friction velocity u_τ/u_{theory} at the three different friction Reynolds numbers $Re_\tau = 1000, 2000, 5200$. Figure 8 demonstrates that u_τ/u_{theory} rapidly converges to the high-accuracy region (shown in yellow, with a relative error of 5%) for all three friction Reynolds numbers at $x/\delta = 2$ to $x/\delta = 4$.

Further investigation of STG is carried out at $Re_\tau = 5200$ for different resolutions of $H = 20, 40, 60$ (LBU), with the first cell y^+ equal
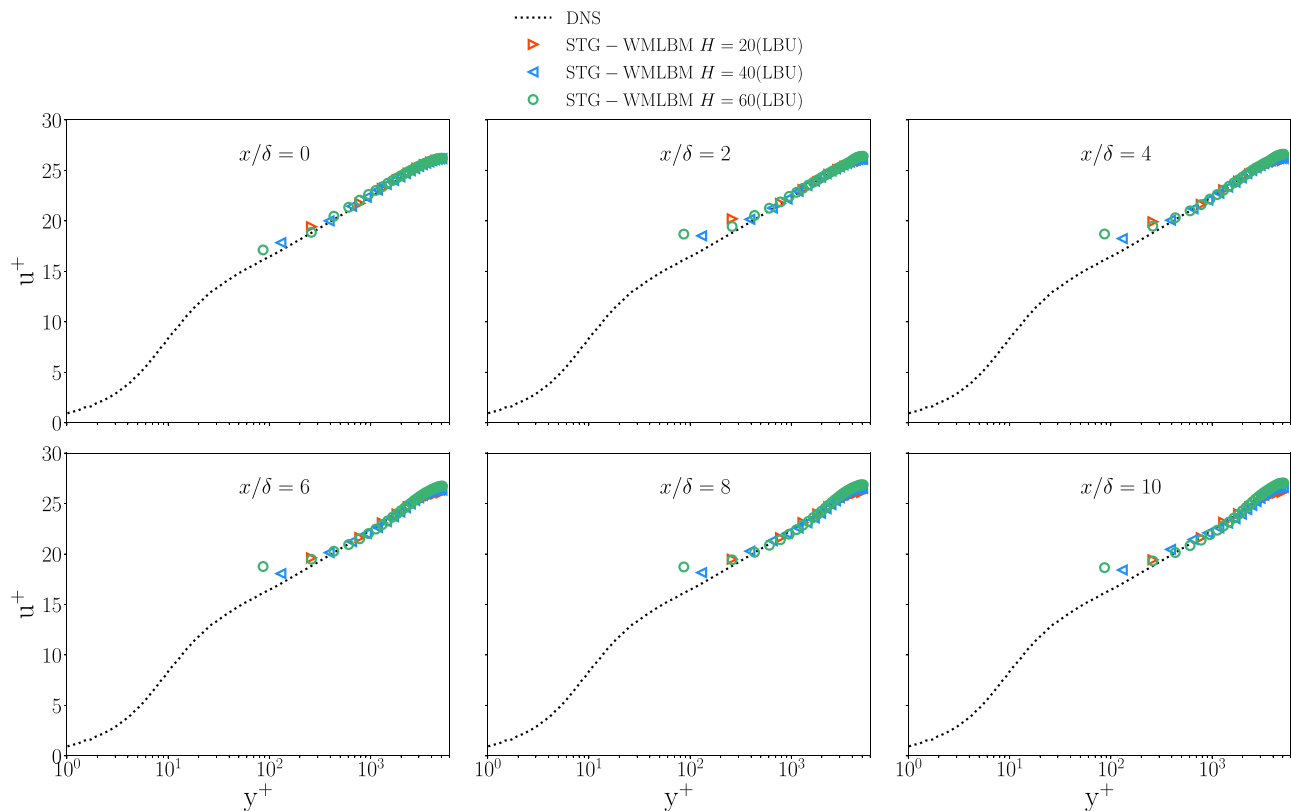

FIG. 9. u^+ as a function of y^+ at $Re_\tau = 5200$ for different resolutions $H = 20, 40, 60$ (LBU).
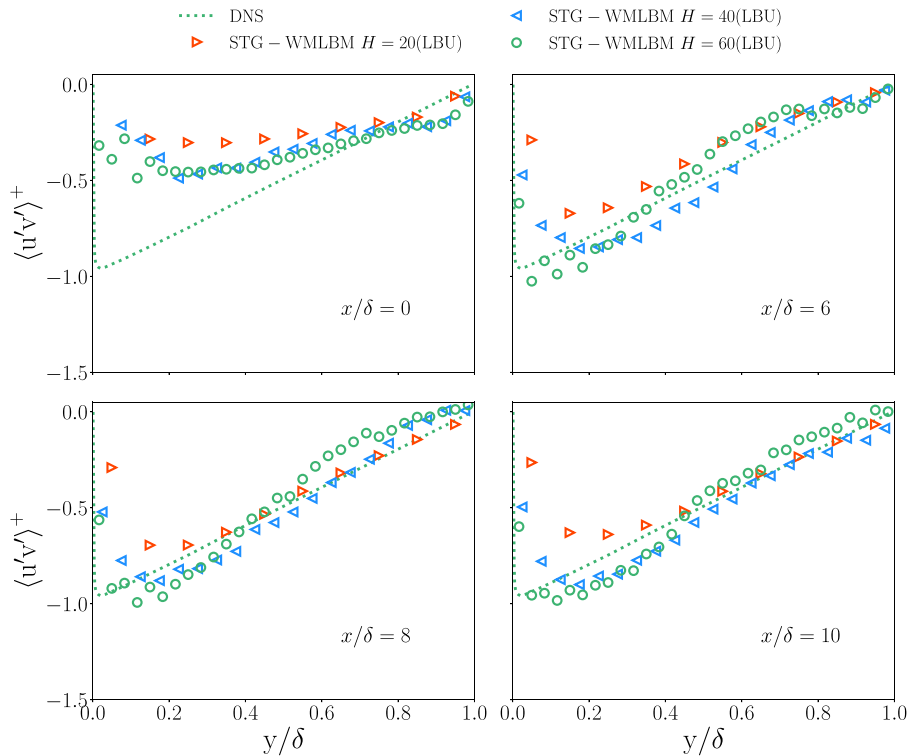
FIG. 10. $\langle u'v' \rangle^+$ as a function of y/δ at $Re_\tau = 5200$ for different resolutions $H = 20, 40, 60$ (LBU).

to $y^+ \approx 260, 130, 86.7$, respectively. Although the first few near-wall cells are slightly off the reference, the STG results match well with DNS further away from the wall; see Fig. 9. In Fig. 9, it can be observed that as the resolution increases, the u^+ values are overestimated when compared to the DNS data at high y^+ values. This phenomenon is a well-known effect in LES modeling named as the log-layer mismatch. The discrepancy may be attributed to the SGS turbulence modeling and the choice of shear estimation from either the first or second near-wall layer. Interested readers can refer to Asmuth *et al.*[44] for a discussion on the choice of shear estimation. Moreover, the results also reveal that at higher resolutions, the first off-wall layer exhibits a greater discrepancy with DNS than at lower resolutions. One possible explanation for this is the use of second-layer shear stress to model the first layer. However, using first-layer information to estimate shear stress may increase the log-layer mismatch.[44,58] Further investigation is required to fully understand this effect.

The analysis of $\langle u'v' \rangle^+$ as a function of y/δ is carried out at all three resolutions. Figure 10 displays the results of the STG data with the DNS reference. The results converge to the DNS reference around $x/\delta = 6$ to $x/\delta = 8$.

V. CONCLUSIONS

This paper presents a synthetic turbulent generator (STG) model based on the LES–LBM framework for high friction Reynolds number simulations ($Re_\tau = 1000, 2000, 5200$). We use wall function based on Reichardt's law[46] in combination with the force-based method, which simplifies the implementation. The STG simulations are examined at different resolutions [$H = 20, 40, 60$ (LBU)] and compared with the

DNS data, showing immediate convergence to the mean velocity field from the inlet of the channel flow. Further analysis of the Reynolds stress indicates that convergence to the DNS data occurs around $x/\delta = 6$ to $x/\delta = 8$. The presented STG model is computationally efficient and quickly converges to the DNS data even at low resolutions, which is promising for high Reynolds-number applications. One interesting future perspective for the presented framework is how to couple the LES–LBM turbulent flow back to RANS. Another future work can be to compare different turbulent generation methods for LBM.

AUTHOR DECLARATIONS
Conflict of Interest

The authors have no conflicts to disclose.

Author Contributions

Xiao Xue: conceptualization (equal); data curation (equal); formal analysis (equal); investigation (equal); methodology (equal); project administration (equal); resources (equal); software (equal); validation

(equal); visualization (equal); writing—original draft (equal); and writing—review and editing (equal). **Hua-Dong Yao:** conceptualization (equal); formal analysis (equal); funding acquisition (equal); project administration (equal); resources (equal); supervision (equal); and writing—review and editing (equal). **Lars Davidson:** conceptualization (equal); formal analysis (equal); investigation (equal); methodology (equal); resources (equal); supervision (equal); and writing—review and editing (equal).

DATA AVAILABILITY

The data that support the findings of this study are available from the corresponding author upon reasonable request.

APPENDIX: D3Q19 MRT MATRIX AND CHOOSE OF PARAMETERS

The MRT matrix $\mathbf{M}$ in Eq. (4) is defined as

$$
\mathbf{M} =
\begin{bmatrix}
1 & 1 & 1 & 1 & 1 & 1 & 1 & 1 & 1 & 1 & 1 & 1 & 1 & 1 & 1 & 1 & 1 & 1 & 1 \\
8 & 8 & -11 & 8 & 8 & 8 & -11 & 8 & -11 & -30 & -11 & 8 & -11 & 8 & 8 & 8 & -11 & 8 & 8 \\
1 & 1 & -4 & 1 & 1 & 1 & -4 & 1 & -4 & 12 & -4 & 1 & -4 & 1 & 1 & 1 & -4 & 1 & 1 \\
0 & -1 & 0 & 1 & 0 & -1 & 0 & 1 & -1 & 0 & 1 & -1 & 0 & 1 & 0 & -1 & 0 & 1 & 0 \\
0 & -1 & 0 & 1 & 0 & -1 & 0 & 1 & 4 & 0 & -4 & -1 & 0 & 1 & 0 & -1 & 0 & 1 & 0 \\
-1 & 0 & 0 & 0 & 1 & -1 & -1 & -1 & 0 & 0 & 0 & 1 & 1 & 1 & -1 & 0 & 0 & 0 & 1 \\
-1 & 0 & 0 & 0 & 1 & -1 & 4 & -1 & 0 & 0 & 0 & 1 & -4 & 1 & -1 & 0 & 0 & 0 & 1 \\
-1 & -1 & -1 & -1 & -1 & 0 & 0 & 0 & 0 & 0 & 0 & 0 & 0 & 0 & 1 & 1 & 1 & 1 & 1 \\
-1 & -1 & 4 & -1 & -1 & 0 & 0 & 0 & 0 & 0 & 0 & 0 & 0 & 0 & 1 & 1 & -4 & 1 & 1 \\
-2 & 1 & -1 & 1 & -2 & 1 & -1 & 1 & 2 & 0 & 2 & 1 & -1 & 1 & -2 & 1 & -1 & 1 & -2 \\
-2 & 1 & 2 & 1 & -2 & 1 & 2 & 1 & -4 & 0 & -4 & 1 & 2 & 1 & -2 & 1 & 2 & 1 & -2 \\
0 & -1 & -1 & -1 & 0 & 1 & 1 & 1 & 0 & 0 & 0 & 1 & 1 & 1 & 0 & -1 & -1 & -1 & 0 \\
0 & -1 & 2 & -1 & 0 & 1 & -2 & 1 & 0 & 0 & 0 & 1 & -2 & 1 & 0 & -1 & 2 & -1 & 0 \\
0 & 0 & 0 & 0 & 0 & 1 & 0 & -1 & 0 & 0 & 0 & -1 & 0 & 1 & 0 & 0 & 0 & 0 & 0 \\
1 & 0 & 0 & 0 & -1 & 0 & 0 & 0 & 0 & 0 & 0 & 0 & 0 & 0 & -1 & 0 & 0 & 0 & 1 \\
0 & 1 & 0 & -1 & 0 & 0 & 0 & 0 & 0 & 0 & 0 & 0 & 0 & 0 & 0 & -1 & 0 & 1 & 0 \\
0 & 1 & 0 & -1 & 0 & -1 & 0 & 1 & 0 & 0 & 0 & -1 & 0 & 1 & 0 & 1 & 0 & -1 & 0 \\
-1 & 0 & 0 & 0 & 1 & 1 & 0 & 1 & 0 & 0 & 0 & -1 & 0 & -1 & -1 & 0 & 0 & 0 & 1 \\
1 & -1 & 0 & -1 & 1 & 0 & 0 & 0 & 0 & 0 & 0 & 0 & 0 & 0 & -1 & 1 & 0 & 1 & -1
\end{bmatrix}. \quad (A1)
$$

The relaxation parameters that are not determined by the viscosity are set to

$$\omega_0 = \omega_3 = \omega_5 = \omega_7 = \omega_1 = 1.0, \quad (A2)$$

$$\omega_1 = 1.19, \quad (A3)$$

$$\omega_2 = \omega_{10} = \omega_{12} = 1.6, \quad (A4)$$

$$\omega_4 = \omega_6 = \omega_8 = 1.2, \quad (A5)$$

$$\omega_{16} = \omega_{17} = \omega_{18} = 1.98. \quad (A6)$$

REFERENCES

[1] F. Porté-Agel, Y.-T. Wu, H. Lu, and R. J. Conzemius, "Large-eddy simulation of atmospheric boundary layer flow through wind turbines and wind farms," J. Wind Eng. Ind. Aerodyn. **99**, 154–168 (2011).

[2] D. R. Chapman, "Computational aerodynamics development and outlook," AIAA J. **17**, 1293–1313 (1979).

[3] H. Choi and P. Moin, "Grid-point requirements for large eddy simulation: Chapman's estimates revisited," Phys. Fluids **24**, 011702 (2012).

[4] J. Smagorinsky, "General circulation experiments with the primitive equations," Mon. Weather Rev. **91**, 99–194 (1963).

[5] M. Germano, U. Piomelli, P. Moin, and W. H. Cabot, "A dynamic subgrid-scale eddy viscosity model," Phys. Fluids A: Fluid Dyn. **3**, 1760–1765 (1991).

[6] P. Sagaut, "Large eddy simulation for incompressible flows," *Scientific Computation* (Springer, Berlin, Heidelberg, 2002).

[7] X. I. Yang and K. P. Griffin, "Grid-point and time-step requirements for direct numerical simulation and large-eddy simulation," Phys. Fluids **33**, 015108 (2021).

[8] X. Xue, L. Biferale, M. Sbragaglia, and F. Toschi, "A lattice Boltzmann study on Brownian diffusion and friction of a particle in a confined multicomponent fluid," J. Comput. Sci. **47**, 101113 (2020).

[9] X. Xue, M. Sbragaglia, L. Biferale, and F. Toschi, "Effects of thermal fluctuations in the fragmentation of a nanoligament," Phys. Rev. E **98**, 012802 (2018).

[10] X. Xue, L. Biferale, M. Sbragaglia, and F. Toschi, "A lattice Boltzmann study of particle settling in a fluctuating multicomponent fluid under confinement," Eur. Phys. J. E **44**, 142 (2021).

[11] D. Chiappini, X. Xue, G. Falcucci, and M. Sbragaglia, "Ligament break-up simulation through pseudo-potential lattice Boltzmann method," AIP Conf. Proc. **1978**, 420003 (2018).

[12] D. Chiappini, M. Sbragaglia, X. Xue, and G. Falcucci, "Hydrodynamic behavior of the pseudopotential lattice Boltzmann method for interfacial flows," Phys. Rev. E **99**, 053305 (2019).

[13] S. Hou, J. Sterling, S. Chen, and G. Doolen, "A lattice Boltzmann subgrid model for high Reynolds number flows," arXiv:comp-gas/9401004 (1994).

[14] F. Toschi and E. Bodenschatz, "Lagrangian properties of particles in turbulence," Annu. Rev. Fluid Mech. **41**, 375–404 (2009).

[15] I. V. Karlin, A. Ferrante, and H. C. Öttinger, "Perfect entropy functions of the lattice Boltzmann method," Europhys. Lett. **47**, 182 (1999).

[16] P. Lallemand and L.-S. Luo, "Theory of the lattice Boltzmann method: Dispersion, dissipation, isotropy, Galilean invariance, and stability," Phys. Rev. E **61**, 6546 (2000).

[17] X. Shao, M. C. Santasmasas, X. Xue, J. Niu, L. Davidson, A. J. Revell, and H.-D. Yao, "Near-wall modeling of forests for atmosphere boundary layers using lattice Boltzmann method on GPU," Eng. Appl. Comput. Fluid Mech. **16**, 2143–2155 (2022).

[18] S. Succi, *The Lattice Boltzmann Equation: For Fluid Dynamics and Beyond* (Oxford University Press, 2001).

[19] T. Krüger, H. Kusumaatmaja, A. Kuzmin, O. Shardt, G. Silva, and E. M. Viggen, *The Lattice Boltzmann Method* (Springer International Publishing, 2017), Vol. 10, p. 978.

[20] P. Lallemand, L.-S. Luo, M. Krafczyk, and W.-A. Yong, "The lattice Boltzmann method for nearly incompressible flows," J. Comput. Phys. **431**, 109713 (2021).

[21] X. Wu, "Inflow turbulence generation methods," Annu. Rev. Fluid Mech. **49**, 23–49 (2017).

[22] J. Schlüter, H. Pitsch, and P. Moin, "Large-eddy simulation inflow conditions for coupling with Reynolds-averaged flow solvers," AIAA J. **42**, 478–484 (2004).

[23] T. S. Lund, X. Wu, and K. D. Squires, "Generation of turbulent inflow data for spatially-developing boundary layer simulations," J. Comput. Phys. **140**, 233–258 (1998).

[24] P. Spalart, M. Strelets, and A. Travin, "Direct numerical simulation of large-eddy-break-up devices in a boundary layer," Int. J. Heat Fluid Flow **27**, 902–910 (2006).

[25] M. Shur, P. R. Spalart, M. Strelets, and A. Travin, "A rapid and accurate switch from RANS to LES in boundary layers using an overlap region," Flow Turbul. Combust. **86**, 179–206 (2011).

[26] F. Mathey, D. Cokljat, J. P. Bertoglio, and E. Sergent, "Assessment of the vortex method for large eddy simulation inlet conditions," Prog. Comput. Fluid Dyn.: Int. J. **6**, 58–67 (2006).

[27] N. Jarrin, R. Prosser, J.-C. Uribe, S. Benhamadouche, and D. Laurence, "Reconstruction of turbulent fluctuations for hybrid RANS/LES simulations using a synthetic-eddy method," Int. J. Heat Fluid Flow **30**, 435–442 (2009).

[28] A. Skillen, A. Revell, and T. Craft, "Accuracy and efficiency improvements in synthetic eddy methods," Int. J. Heat Fluid Flow **62**, 386–394 (2016).

[29] B. Roidl, M. Meinke, and W. Schröder, "Zonal RANS-LES computation of transonic airfoil flow," AIAA Paper No. 2011-3974, 2011, p. 3974.

[30] B. Roidl, M. Meinke, and W. Schröder, "A zonal RANS–LES method for compressible flows," Comput. Fluids **67**, 1–15 (2012).

[31] M. L. Shur, P. R. Spalart, M. K. Strelets, and A. K. Travin, "Synthetic turbulence generators for RANS-LES interfaces in zonal simulations of aerodynamic and aeroacoustic problems," Flow Turbul. Combust. **93**, 63–92 (2014).

[32] M. L. Shur, P. R. Spalart, M. K. Strelets, and A. K. Travin, "A hybrid RANS-LES approach with delayed-DES and wall-modelled LES capabilities," Int. J. Heat Fluid Flow **29**, 1638–1649 (2008).

[33] Y. Koda and F.-S. Lien, "The lattice Boltzmann method implemented on the GPU to simulate the turbulent flow over a square cylinder confined in a channel," Flow Turbul. Combust. **94**, 495–512 (2015).

[34] H. Nakayama, N. Onodera, D. Satoh, H. Nagai, Y. Hasegawa, and Y. Idomura, "Development of local-scale high-resolution atmospheric dispersion and dose assessment system," J. Nucl. Sci. Technol. **59**, 1314–1329 (2022).

[35] H. Asmuth, G. P. N. Diaz, H. A. Madsen, E. Branlard, A. R. M. Forsting, K. Nilsson, J. Jonkman, and S. Ivanell, "Wind turbine response in waked inflow: A modelling benchmark against full-scale measurements," Renewable Energy **191**, 868–887 (2022).

[36] E. Buffa, J. Jacob, and P. Sagaut, "Lattice-Boltzmann-based large-eddy simulation of high-rise building aerodynamics with inlet turbulence reconstruction," J. Wind Eng. Ind. Aerodyn. **212**, 104560 (2021).

[37] S. Fan, M. C. Santasmasas, X.-W. Guo, C. Yang, and A. Revell, "Source term-based turbulent flow simulation on GPU with link-wise artificial compressibility method," Int. J. Comput. Fluid Dyn. **35**, 549–561 (2021).

[38] X. Xue, H.-D. Yao, and L. Davidson, "Synthetic turbulence generator for lattice Boltzmann method at the interface between RANS and LES," Phys. Fluids **34**, 055118 (2022).

[39] O. Malaspinas and P. Sagaut, "Wall model for large-eddy simulation based on the lattice Boltzmann method," J. Comput. Phys. **275**, 25–40 (2014).

[40] A. Musker, "Explicit expression for the smooth wall velocity distribution in a turbulent boundary layer," AIAA J. **17**, 655–657 (1979).

[41] M. Haussmann, A. C. Barreto, G. L. Kouyi, N. Rivière, H. Nirschl, and M. J. Krause, "Large-eddy simulation coupled with wall models for turbulent channel flows at high Reynolds numbers with a lattice Boltzmann method: Application to Coriolis mass flowmeter," Comput. Math. Appl. **78**, 3285–3302 (2019).

[42] H. Maeyama, T. Imamura, J. Osaka, and N. Kurimoto, "Unsteady turbulent flow simulation using lattice Boltzmann method with near-wall modeling," AIAA Paper No. 2020-2565, 2020, p. 2565.

[43] S. Wilhelm, J. Jacob, and P. Sagaut, "A new explicit algebraic wall model for LES of turbulent flows under adverse pressure gradient," Flow Turbul. Combust. **106**, 1–35 (2021).

[44] H. Asmuth, C. F. Janßen, H. Olivares-Espinosa, and S. Ivanell, "Wall-modeled lattice Boltzmann large-eddy simulation of neutral atmospheric boundary layers," Phys. Fluids **33**, 105111 (2021).

[45] Y. Kuwata and K. Suga, "Wall-modeled large eddy simulation of turbulent heat transfer by the lattice Boltzmann method," J. Comput. Phys. **433**, 110186 (2021).

[46] H. Reichardt, "Vollständige darstellung der turbulenten geschwindigkeitsverteilung in glatten leitungen," ZAMM-J. Appl. Math. Mech./Z. Angew. Math. Mech. **31**, 208–219 (1951).

[47] S. Hoyas and J. Jiménez, "Scaling of the velocity fluctuations in turbulent channels up to $Re_\tau = 2003$," Phys. Fluids **18**, 011702 (2006).

[48] M. Lee and R. D. Moser, "Direct numerical simulation of turbulent channel flow up to $Re_\tau \approx 5200$," J. Fluid Mech. **774**, 395–415 (2015).

[49] W. Yang, Y. Liu, E. Deng, Y. Wang, X. He, M. Lei, and Y. Zou, "Field test and numerical reconstitution of natural winds at the tunnel entrance section of high-speed railway," Int. J. Numer. Methods Heat Fluid Flow **33**, 617 (2023).

[50] W. Yang, H. Yue, E. Deng, Y. Wang, X. He, and Y. Zou, "Influence of the turbulence conditions of crosswind on the aerodynamic responses of the train when running at tunnel-bridge-tunnel," J. Wind Eng. Ind. Aerodyn. **229**, 105138 (2022).

[51] D. d'Humieres, "Multiple–relaxation–time lattice Boltzmann models in three dimensions," Philos. Trans. R. Soc. London, Ser. A **360**, 437–451 (2002).

[52] Z. Guo, C. Zheng, and B. Shi, "Discrete lattice effects on the forcing term in the lattice Boltzmann method," Phys. Rev. E **65**, 046308 (2002).

[53] A. Pasquali, M. Geier, and M. Krafczyk, "Near-wall treatment for the simulation of turbulent flow by the cumulant lattice Boltzmann method," Comput. Math. Appl. **79**, 195–212 (2020).

[54] D. C. Wilcox, "Reassessment of the scale-determining equation," AIAA J. **26**, 1299–1310 (1988).

[55] S. Wallin and A. V. Johansson, "A new explicit algebraic Reynolds stress model for incompressible and compressible turbulent flows," J. Fluid Mech. **403**, 89–132 (2000).

[56] J. Latt, B. Chopard, O. Malaspinas, M. Deville, and A. Michler, "Straight velocity boundaries in the lattice Boltzmann method," Phys. Rev. E **77**, 056703 (2008).

[57] Q. Zou and X. He, "On pressure and velocity boundary conditions for the lattice Boltzmann BGK model," Phys. Fluids **9**, 1591–1598 (1997).

[58] S. Kawai and J. Larsson, "Wall-modeling in large eddy simulation: Length scales, grid resolution, and accuracy," Phys. Fluids **24**, 015105 (2012).